Computational Geosciences (2006) 10:221–240
DOI: 10.1007/s10596-005-9020-4

Numerical simulation of debris flow with application on hazard area mapping

Ko-Fei Liu[a] and Ming Chung Huang[b]

[a]*Department of Civil Engineering, National Taiwan University, No. 1 Section 4, Roosevelt Road, Taipei 106, Taiwan.*
E-mail: kfliu@ntu.edu.tw
[b]*Ching-Yun Technology University, Chung-Li, Taiwan.*

Accepted 4 August 2005

A numerical program developed for field application is presented in this paper. We use the generalized Julien and Lan [8] rheological model to simulate debris flows. Due to the derivative discontinuous nature of the constitutive law, flow is separated into plug region and bottom region (with stress greater than yield stress). The program solves the plug flow layer solution first, and then corrects the solution with the bottom layer approximation. Numerical scheme with upwind method and central difference in space and Adam–Bashforth third-order scheme in time is used for both layers. The scheme is tested against analytical solutions and laboratory experiments with very good results. Application to a field case with more complicated geometry also achieves good agreement, with error less than 5% compared to field measurements. The final example demonstrates how this numerical program is used in a preliminary design.

Keywords: debris flows, numerical simulation, debris flow hazard zone, yield stress, debris flow mapping

1. Introduction

Debris flows are a frequent phenomenon in Taiwan. To minimize the possible hazard caused by debris flows, normal countermeasures include constructing dams, land-use limitation, or habitant evacuation. One of the common uncertainties during planning any countermeasures is the hazard zone coverage and the path of debris flows. A numerical model suitable for dynamic simulation of field cases is a very useful tool for engineering designs and evaluation of their effectiveness. This research aims at developing such a tool.

Many researchers developed numerical models to simulate debris flows under different situations. Steady flow solutions with a yield stress were studied by Johnson [7], Liu and Mei [12], and Coussot and Proust [4]. Liu and Mei [12] and Ng and Mei

[16] also studied roll waves for mudflows. Huang and Garcia [5] studied two-dimensional, slow unsteady flow from constant source and used matched-asymptotic perturbation to patch the wave front. Balmforth and Liu [2] used the Herschel–Bulkley constitutive law to study two-dimensional fluid film falling down an inclined plane and determined the critical Reynolds number for the onset of roll waves. Mei and Yuhi [15] studied three-dimensional slow flow in elliptic channel and found the dead zone within the cross section. Iverson et al. [6] used a two-phase flow model to simulate debris flows flowing from a large-scale flume (5×100 m) to a wide deposition basin. Models used for debris-flow simulation are usually depth-averaged two-dimensional models. Most of the above studies focused on laboratory-scale experiments or slow debris flow motion in regular channels. However, debris flows in the field have length and velocity scales several orders larger than those in the laboratory. Combined with the complicated geometry, the phenomenon in the field is quite different from that in a controlled environment.

O'Brien and Julien [17] used the Julien and Lan [8] model to simulate hyperconcentrated sediment flow and developed the commercial software FLO-2D. FLO-2D uses 2-D kinematic equations and a central difference routing scheme. It is a dynamic routing model that does not have the capacity to deal with shock conditions. Tsai [19] used a staggered grid scheme with Bagnold's constitutive law [1] to develop a numerical program, but the computation of flow has to be terminated when the total volume of debris flow specified from the boundaries reaches a predetermined volume.

2. Governing equations

The x-axis coincides with the averaged bottom of the channel and is inclined at an angle θ with respect to the horizon. The y-axis is in the transverse direction and z-axis is perpendicular to both x- and y-axes. The governing equations are the continuity equation and momentum equations.

2.1. Constitutive relation

The constitutive relation proposed by Julien and Lan [8] is used here. The original one-dimensional version is extended to three-dimensional as

$$\tau_{ij} = \left(\frac{\tau_0}{\varepsilon_{II}} + \mu_d + \mu_c \varepsilon_{II}\right)\varepsilon_{ij} \quad \text{for} \quad \tau_{II} > \tau_0 \tag{1a}$$

$$\varepsilon_{ij} = 0 \quad \text{for} \quad \tau_{II} < \tau_0 \tag{1b}$$

where τ_{ij} is the stress tensor and ε_{ij} is the strain rate tensor, τ_0 is the yield stress, μ_d is the dynamic viscosity and μ_c is turbulent–dispersive parameter. τ_{II} and ε_{II} represent the second invariant of the stress and strain rate tensor, respectively. Intuitively, this model, which includes the viscous effect (μ_d) and dispersive stress (μ_c) effect, could be used for m0udflows and granular flows.

In fluid mechanics, the boundary layer represents a thin layer near the physical boundary and is characterized by its strong shear effect. This layer is so thin that if included in a numerical computation it usually leads to unreasonable small mesh size or instability for the numerical schemes. Therefore, it is customary to separate the calculation of the main flow with its boundary layer. We shall adopt this concept in the simulation of debris flows.

Let us define the lower portion of debris flow which has stress greater than the yield stress as the "bottom layer" and denote the thickness as $\delta(x, y, t)$. The depth ratio between the "bottom layer" and the main debris flow can be proved to be small in many occasions [10,11]. The separation of the whole flow into two layers is not only physically reasonable but also suggested by the discontinuity in the constitutive law at $\tau_{II} = \tau_0$. Unless the constitutive law is modified, the numerical treatment for different region has to be different. In what follows, our discussion and numerical treatment for plug region and bottom region are separated.

2.2. Governing equations

Debris flows, in a laboratory or in the field, can usually be considered as long waves, i.e., the depth scale is much smaller than the horizontal length scales. If we invoke this long wave assumption into equation (1b), we obtain

$$\begin{aligned}\varepsilon_{II} &= \left(\frac{1}{2}\varepsilon_{ij}\varepsilon_{ij}\right)^{1/2} = \left[2\left(\frac{\partial u}{\partial x}\right)^2 + 2\left(\frac{\partial v}{\partial y}\right)^2 + 2\left(\frac{\partial w}{\partial z}\right)^2 + \left(\frac{\partial u}{\partial y} + \frac{\partial v}{\partial x}\right)^2 + \left(\frac{\partial u}{\partial z} + \frac{\partial w}{\partial x}\right)^2 + \left(\frac{\partial v}{\partial z} + \frac{\partial w}{\partial y}\right)^2\right]^{1/2} \\ &= \left[2\left(\frac{\partial u}{\partial x}\right)^2 + 2\left(\frac{\partial v}{\partial y}\right)^2 + 2\left(\frac{\partial w}{\partial z}\right)^2 + \left(\frac{\partial u}{\partial y}\right)^2 + 2\left(\frac{\partial u}{\partial y}\right)\left(\frac{\partial v}{\partial x}\right) + \left(\frac{\partial v}{\partial x}\right)^2 + \left(\frac{\partial u}{\partial z}\right)^2 + 2\left(\frac{\partial u}{\partial z}\right)\left(\frac{\partial w}{\partial x}\right)\right. \\ &\quad \left. + \left(\frac{\partial w}{\partial x}\right)^2 + \left(\frac{\partial v}{\partial z}\right)^2 + 2\left(\frac{\partial v}{\partial z}\right)\left(\frac{\partial w}{\partial y}\right) + \left(\frac{\partial w}{\partial y}\right)^2\right]^{1/2} = 0 \end{aligned} \tag{2}$$

where u, v, w are velocity components in x-, y-, z-directions, respectively. Since derivatives in x- or y-direction is much smaller than vertical derivatives, we obtain from equation (2) by neglecting small terms

$$\frac{\partial u}{\partial z} = 0, \frac{\partial v}{\partial z} = 0 \tag{3}$$

This implies that the portion of debris flow near the free surface where the stress-free condition applies is a two-dimensional plug flow, i.e., $u \neq u(z)$ and $v \neq v(z)$. We define the bottom of the debris flow as $z = B(x, y, t)$, where t represents time. Substituting (3)

into momentum equations for the plug flow region ($\tau_{II} < \tau_0$) and integrating the continuity equation, x and y momentum equations from the bottom $z = B(x, y, t) + \delta(x, y, t)$ to the free surface $z = h(x, y, t)$, we obtain in conservative form

$$\frac{\partial H}{\partial t} + \frac{\partial (uH)}{\partial x} + \frac{\partial (vH)}{\partial y} = 0 \tag{4}$$

$$\frac{\partial (uH)}{\partial t} + \frac{\partial (u^2 H)}{\partial x} + \frac{\partial (uvH)}{\partial y} = -g \cos\theta H \frac{\partial B}{\partial x} - g \cos\theta H \frac{\partial H}{\partial x} + g \sin\theta H - \frac{1}{\rho} \times \frac{\tau_0 u}{\sqrt{u^2 + v^2}} \tag{5}$$

$$\frac{\partial (vH)}{\partial t} + \frac{\partial (uvH)}{\partial x} + \frac{\partial (v^2 H)}{\partial y} = -g \cos\theta H \frac{\partial B}{\partial y} - g \cos\theta H \frac{\partial H}{\partial y} - \frac{1}{\rho} \frac{\tau_0 v}{\sqrt{u^2 + v^2}} \tag{6}$$

where $H = h(x, y, t) - B(x, y, t) - \delta(x, y, t)$ is the plug flow depth.

With zero pressure at the free surface $z = h(x, y, t)$, z momentum leads to static pressure

$$p = \rho g \cos\theta (h - z) \tag{7}$$

The bottom erosion or deposition is neglected in (4). In the derivation of (5) and (6), the direction of stress is expressed with the velocity components. Equations (4), (5) and (6) can be used to solve the three unknowns H, u and v. However, the real flow depth h can be found only if the boundary layer depth δ is known. Since the only feedback from the bottom layer to the plug region is the bottom layer thickness δ, we can adopt the momentum integral method to bottom layer and focus on solving δ.

Substituting (1a) into stress terms in momentum equations, multiplying u with x-momentum equation and v with y-momentum equation, and adding the results, we obtain

$$\begin{aligned} &\frac{1}{2}\left\{\frac{\partial (u_b^2 + v_b^2)}{\partial t} + \frac{\partial u_b (u_b^2 + v_b^2)}{\partial x} + \frac{\partial v_b (u_b^2 + v_b^2)}{\partial y} + \frac{\partial w_b (u_b^2 + v_b^2)}{\partial z}\right\} \\ &\quad = -g \cos\theta \left\{u_b \frac{\partial h}{\partial x} + v_b \frac{\partial h}{\partial y}\right\} + g \sin\theta u + \frac{1}{\rho} \frac{\partial}{\partial z}\left\{u_b \tau_{zx} + v_b \tau_{zy}\right\} \\ &\qquad - \frac{1}{\rho}\left\{\tau_{zx} \frac{\partial u_b}{\partial z} + \tau_{zy} \frac{\partial v_b}{\partial z}\right\} \end{aligned} \tag{8}$$

where u_b and v_b are the velocities in the "bottom layer." The boundary conditions are

$$u_b = v_b = 0 \qquad z = B \qquad \text{no slip condition} \tag{9}$$

$$u_b = u,\ v_b = v \qquad z = B + \delta \quad \text{continuity of velocities} \tag{10}$$

$$\frac{\partial u_b}{\partial z} = 0 \qquad z = B + \delta \quad \text{definition of the bottom layer} \tag{11}$$

With the momentum integral method, the velocity profile can be assumed as

$$\frac{v_b}{v} = \frac{u_b}{u} = 2\left(\frac{z-B}{\delta - B}\right) - \left(\frac{z-B}{\delta - B}\right)^2 \tag{12}$$

which satisfies the boundary conditions (9), (10) and (11). Substituting (12) into (8) and integrating from z = B (bottom) to $z = B + \delta$, (8) becomes

$$\begin{aligned} &\frac{4}{15}\frac{\partial \delta(u^2+v^2)}{\partial t} + \frac{8}{35}\frac{\partial \delta u(u^2+v^2)}{\partial x} + \frac{8}{35}\frac{\partial \delta v(u^2+v^2)}{\partial y} \\ &= -\frac{2}{3}g\cos\theta\delta\left[u\frac{\partial B}{\partial x} + v\frac{\partial B}{\partial y}\right] - \frac{2}{3}g\cos\theta\delta\left[u\frac{\partial H}{\partial x} + v\frac{\partial H}{\partial y}\right] \\ &\quad + \frac{2}{3}g\sin\theta\delta u - \frac{4}{3}\frac{\mu_d(u^2+v^2)}{\rho\delta} - 2\frac{\mu_c(u^2+v^2)^{3/2}}{\rho\delta^2} \end{aligned} \tag{13}$$

where the kinematic boundary conditions have been used.

The final set of governing equations is composed of equations (4–6) and (13). Unknowns are u, v, H and δ. After the velocity field is solved, the impact force can be computed with equations given by Liu and Lee [13].

2.3. *Starting condition and yield stress measurement*

If debris flow starts from a stationary pile of mass, it can flow only if gravity and pressure gradient overcome the bottom yield stress. Therefore, the starting condition can be obtained by setting all velocities to be zero in (5) and (6) and then adding the square of x- and y-momentum to reach

$$\left(\frac{\partial h}{\partial x} - \tan\theta\right)^2 + \left(\frac{\partial h}{\partial y}\right)^2 > \frac{\tau_0^2}{\rho^2 g^2 \cos^2\theta H^2} \tag{14}$$

If a 1-D debris pile is everywhere on the threshold of motion, the profile of the pile can be obtained by replacing the greater sign by an equal sign in (14) and integrating in x to obtain

$$h + \frac{\tau_0}{\rho g \sin\theta} \ln\left(h - \frac{\tau_0}{\rho g \sin\theta}\right) = \tan\theta x + C \tag{15}$$

This equation is used in our laboratory to determine the yield stress of any field material. A pile of field sample is slowly and steadily pushed from the upstream by a vertical plate in a flume. The resulting profile is measured and the yield stress is fitted with equation (15) as in figure 1. This method is good for samples with fine sand or clayey material because water content can be varied. With coarser material, only dry or wetted samples can be tested since water flows within the porous media easily. As a result, the yield stress of in situ sample at different water content can not be measured.

2.4. Other rheological parameter measurements

With field samples being full of granular material, we use a rotating drum to measure τ_0, μ_d and μ_c. The drum (figure 2) is similar to the set-up in Longo and Lamberti [14], but with a modified theory [3]. During the experiments, the drum rotates counterclockwise. There is a region that is carried by the rotating bottom wall towards the upper right. The region adjacent to free surface will move in the opposite direction. We denote the whole depth as h and the wall region depth as H.

The outer diameter of the drum is 2 m and the central rotating cylinder has a diameter of 0.2 m. So the maximum flow depth h allowed in the drum is 1.8 m before the central cylinder interferes with the flow. The width is 0.5 m so that the field sample can be put in.

Whole flow depth h and wall region depth H vary in space. During the experiment, however, only the maximum value at the center is measured. The equations for calibrating rheological parameters at steady state with the maximum flow depths are [3].

$$\rho g(R-H)\sin\theta = -\frac{\tau_0}{h}(2R-h) \tag{16}$$

$$(H-h)\left(2h^2 - Rh + HR - 2R^2\right)\mu_d + 2R(R-h)(R-H)\ln\left(\frac{R-H}{R-h}\right) + \frac{\mu_c U H h}{\tau_0} = 0 \tag{17}$$

With

$$(R-H+2h) - 2R\ln\left(\frac{R-H}{R-h}\right) = 0 \tag{18}$$

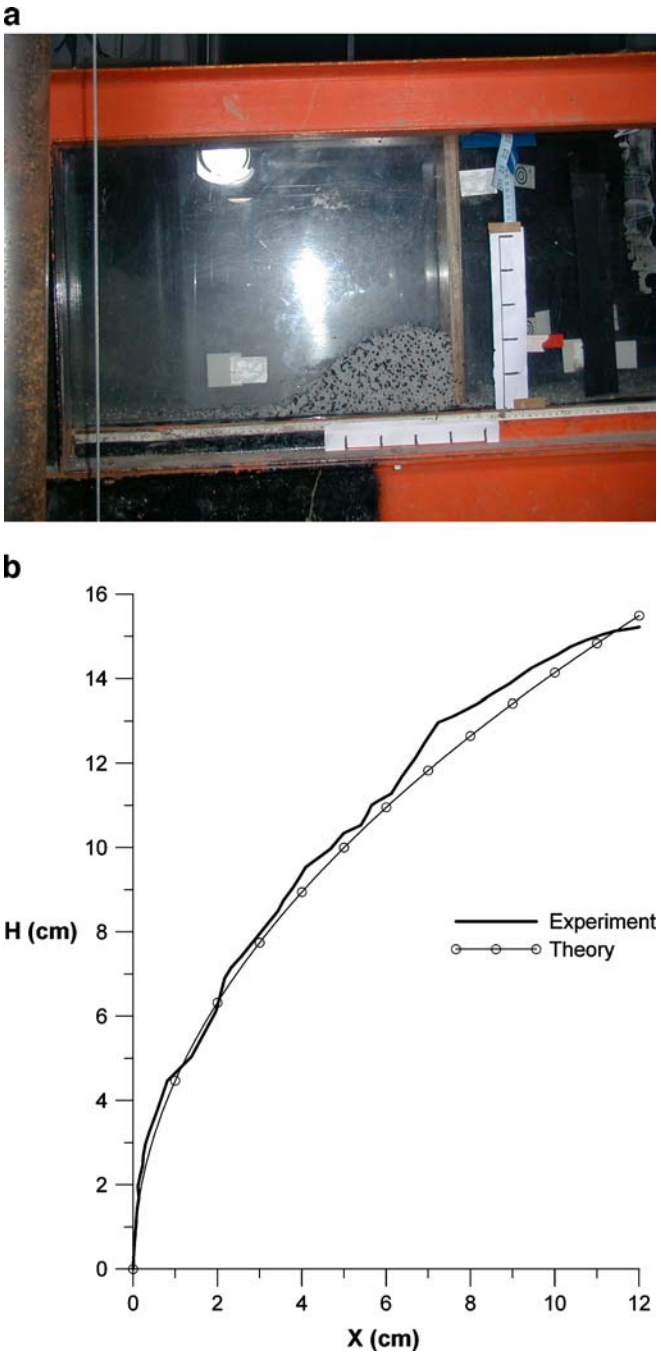

Figure 1. Measuring yield stress with equation (15). (a) Sand pile is pushed slowly from the right with a plate perpendicular to bottom. (b) A sample result is shown for $\tau/\rho g$ = 10.0, Standard deviation is 0.21 cm.

Figure 2. The rotating drum used to measure μ_d, μ_c and τ_0. θ is defined as shown.

where R is the radius and U is the speed at the rim. Along with the measured *maximum* h, H can be calculated from (18) and then τ_0 from (16). After conducting experiments with several different speeds (U), μ_d and μ_c can be calibrated from (17).

Field samples usually have large boulders. In order to use the present equipment, we removed the largest boulders and stones, then collected 1-m^3 sample from the field. Representative values of the field rheological parameters are obtained by averaging calibrated results from different parts of the sample. The obtained result is acceptable only if the value of yield stress is within 20% error of that measured using the method described in section 2.3.

3. Numerical scheme

We use the Adams–Bathforth third-order scheme in time and central difference and upwind scheme in space. Upwind method is used for convective terms. Central difference is used for all the other terms.

Mathematically, one condition for H, u, v and δ each in physical boundary is needed. For debris-flow simulation in the field, it is usually necessary to find a computational domain, which contains the whole reach of the debris flow. In such cases, we can use

$$H = 0, u = 0, v = 0, \delta = 0 \qquad \text{on all boundaries} \tag{19}$$

If debris flows are restrained in a fixed domain such as in a flume, we use no normal flux condition on all physical boundaries. The tracking of points with velocity near zero is important. Overshooting of physical quantities is corrected at every time step.

Because of the nature of constitutive law, velocities are not allowed to change sign within one time step.

The procedure for solving the unknowns in every time step is iterative. u, v, and H are first solved from (4), (5) and (6) assuming $\delta = 0$. The result is then used in (13) to calculate δ. The obtained δ is substituted into (4), (5) and (6) in an iterative manner. If the bottom layer thickness is small compared with the whole flow depth (less than 30%), this process converges after one iteration for 1% precision requirement. If the bottom layer thickness is comparable to the whole depth, 1% precision may require six iterations. In view of the estimation in Liu and Lai [11] that the ratio between bottom layer thickness and the whole depth (δ/H) is usually very small in the field and in many laboratory cases but may occasionally reach 40% in laboratory experiments, this program will have better performance for field simulation or thick debris flows.

The benefit of separating the whole debris flow into two layers is to avoid the necessity of using very fine mesh vertically because of the large strain rate. This can save a lot of CPU time. This is similar to treating boundary layer separately in fluid mechanics calculation. For cases where the bottom layer is thin, neglecting the bottom layer depth in equations (4), (5) and (6) can lead to 10% error or less. Thus the yield stress effect dominates. But for cases where the bottom layer is not thin, this scheme takes as many as 10 iterations to converge, so the CPU benefit may not exist.

Note that, the total energy dissipation in the plug region is $\frac{\partial H(u^2+v^2)}{\partial t}$ and the energy damping of the bottom layer is $\frac{\partial \delta(u_b^2+v_b^2)}{\partial t}$. Since velocities are of the same order, the energy dissipation can be seen proportional to the depth ratio. If the bottom region is thin, the corresponding energy dissipation should be much less than the energy dissipated by yield stress from equations (5) and (6).

The front position is traced carefully. Two possible sources of error need to be considered. If the front is a shock, equation (14) is conservative and the front can be traced by numerical scheme. If debris flows are traveling in a dry bed or in a channel with little deposition, the front depth is zero. In every time step, H will be calculated from (4). Then u and v can be calculated by dividing results of uH and vH from (5) and (6) by H. Under dry bed condition the front flow depth is zero, so the numerical results may diverge rapidly. This is similar to many dry bed problems in water flow problems. In our formulation, the starting condition (14) indicates that the slope of debris flow

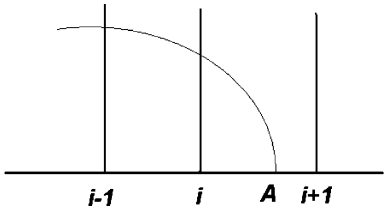

Figure 3. The front position for debris flow traveling at dry bed is denoted by point A. The position is calculated with flow depth at grid i and $i - 1$ and infinite slope at A.

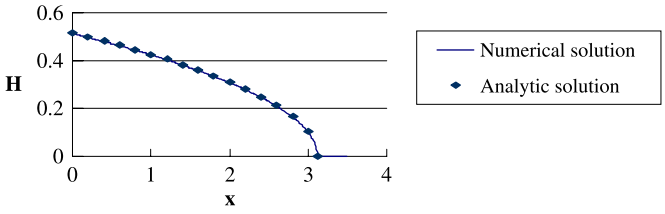

Figure 4. Comparison of 1-D case for the final depth between numerical and analytic solutions. H and x are normalized with respect to initial depth.

has to be very large as flow depth and velocity approach zero. The accuracy of flow depth near dry bed front has to be checked. The quadratic profile with vertical slope is used to approximate the front position, as shown in figure 3.

4. Verification of the numerical scheme

4.1. Verification with the final deposit profile using analytical solutions

Under slow mud motion, the analytical solutions for the final profile of debris flow can be obtained. The final profile for one-dimensional flow is [12]

$$H^2 = \pm\frac{2\tau_0}{\rho g}x + \text{constant} \tag{20}$$

The initial profile is a triangular pile against left wall ($x = 0$) with $H = 1$. The final profile is compared with analytical results (dotted line in figure 4). With $\Delta x = 0.1$, the maximum error is 1%.

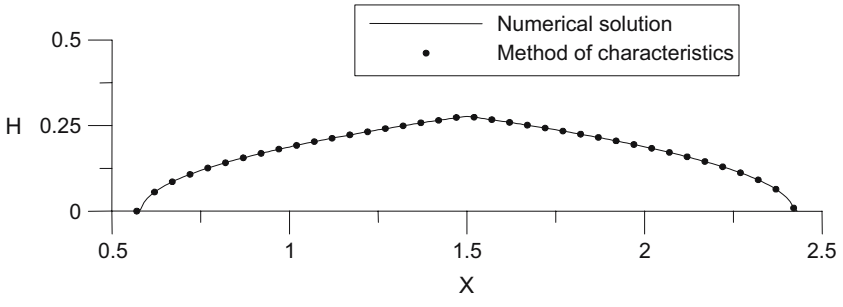

Figure 5. Comparison of final depth at the central cross-section for a 2-D pile between numerical and analytic solutions using method of characteristics. The initial profile is described by equation (21).

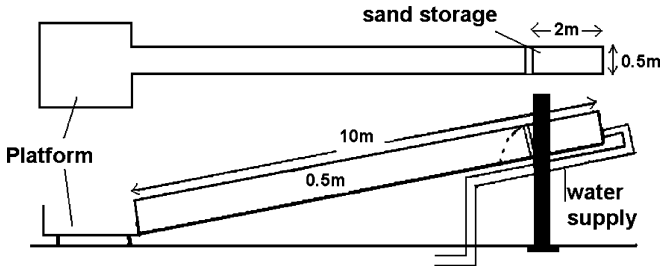

Figure 6. Experimental setup.

For two-dimensional flow, analytical solution with the help of the method of characteristic is also possible [9]. An initial hump with the shape

$$H = 0.5 - (x - 1.5)^2 - (y - 1.5)^2 \tag{21}$$

is used. The comparison between numerical and analytical results at the central cross section is plotted in figure 5. With $\Delta x = \Delta y = 0.01$ and $\Delta t = 0.001$ the maximum error is 0.1%.

4.2. *Verification with flume test results*

A flume 10 m long, 0.5 m wide and 0.5 m high (figure 6) is used in all runs. The angle of the flume can be varied between 0° and 30°. Wood strips, 0.2 cm high, are distributed in 50-cm spacing to increase the flume bottom friction. A horizontal deposition platform of 3 × 3 m is attached at the end of the flume. Test material is sieved from natural sands with 2.5-mm diameter. Using the method described in section 2.3, the yield stress is 90 kPa. Using the method described in section 2.4, μ_d and μ_c are 0.35 poise and 0.003 g/cm, respectively. A total of 390 kg of sand is piled up at the top portion of the flume behind a gate. A water flow of 0.012 m^3/s is used. At the start of the experiments, the gate is opened and debris are released as debris flow.

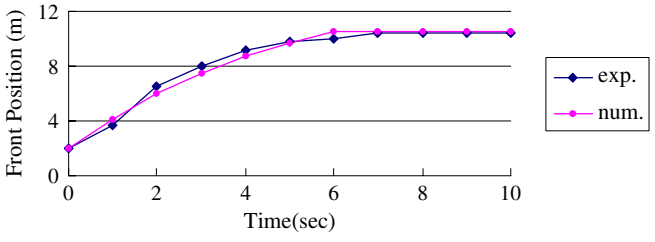

Figure 7. Comparison between the numerically calculated front position and the experimentally measured front position. Error for the final position is 0.1 m.

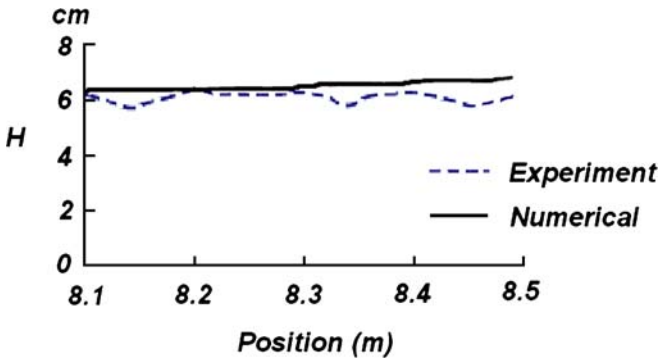

Figure 8. Comparison between the numerically calculated flow depth and the experimentally measured flow depth. The maximum error is 1.1 cm. Position represents the distance to gate. Time is 5 s after gate opened.

Two CCD cameras were used to track the debris flows: one from the top to track the front positions, and another from the side to capture the variation of flow depth. Numerical simulation is carried out with the above parameters without further calibration. The computed and experimentally measured results are compared in figure 7 for the temporal variation of the front position, and in figure 8 for a snapshot of the spatial variation of flow depth. The error for final front position is 0.2%, while the maximum error in the temporal variation is 4%. The maximum error for depth profile in figure 8 is 1.1 cm and roughly 18% error. This error is mostly attributable to the irregular surface of natural debris flow.

In order to test the effect of μ_d and μ_c, we vary their value by a factor of 10. The results are listed in table 1.

4.3. *Field verification – Shen-Mu village in Nan-Tou County, Taiwan*

Shen-Mu village is located within Nan-Tou County. Serious debris flows occurred on July 31, 1996, during Typhoon Herb. The village is in the Hsu-Sui river

Table 1
Bottom layer thickness effect.

μ_d (poise)	μ_c (g/cm)	Variation	Flow depth (cm) at 8.5 m from gate	Final front (m)
3.5	0.003	10 μ_d	6.45	9.94
0.35	0.003	Parameters used	6.23	10.38
0.35	0.03	10 μ_c	6.32	10.23
3.5	0.03	10 μ_d and 10 μ_c	6.62	9.88

The maximum error for varying μ_c and μ_d is only 5% in the final front position. This shows that μ_d and μ_c are not very sensitive in the calculation because of the thin bottom layer.

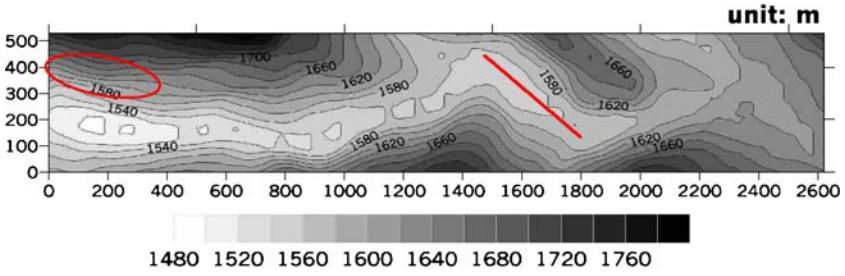

Figure 9. Topographic contour map of Shen-Mu village. The straight line is the cross-section where numerical results are compared with measured final deposition depth in figure 11. The initial debris mass located in the elliptic area marked on the left.

basin. River length is roughly 5 km and the average bottom slope is 11.5°. The topographic contours are plotted in figure 9. The deposition material is mostly clayey sand. According to the investigation by the Disaster Prevention Research Center of National Cheng-Kung University, Taiwan, the volume of the total debris flow deposited is about 560,000 m^3 and the dry specific gravity is 1.3. In order to simulate the flow, we distributed the total (560,000 m^3) debris volume over the upstream source area marked by an ellipse on the left side of figure 9. Yield stress (1,150 N/m^2) was measured in the laboratory via the method described in sections 2.3 and 2.4. Computation grid size is 10 × 10 m. The time step used in the computation was 0.1 s. There is no other source of debris flow material available and no erosion of the original bed throughout that event. Boundary conditions used are no-flow conditions at mountain peak.

The calculated final deposition profile is plotted in figure 10. The solid boundary lines indicates the deposition boundary measured in the field after the disaster. Depth contours are numerically calculated results. The distribution is very close to the

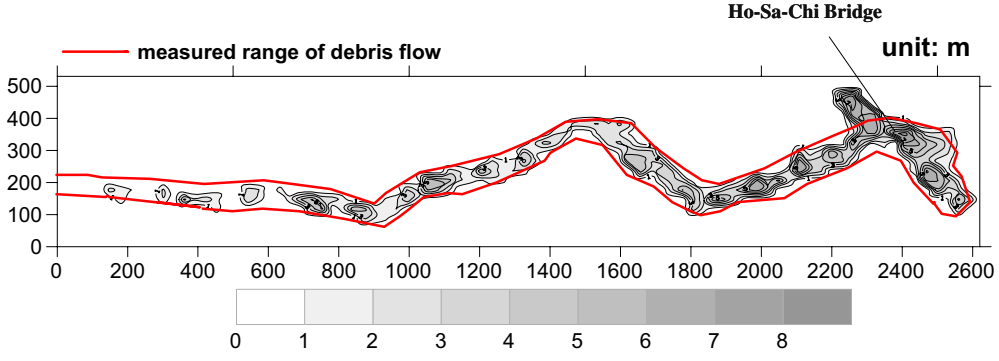

Figure 10. Comparison of simulated and measured boundary of debris flow.

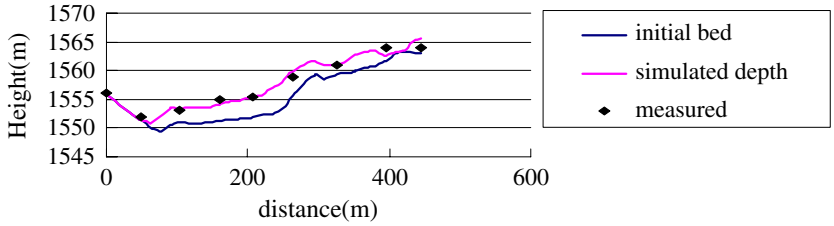

Figure 11. Comparison of simulated and measured depth for final debris flow deposition along the solid line in figure 9. The lower solid line is the bed elevation before disaster; the upper solid line is the numerical calculated free surface after disaster. Dots are measured height just after disaster.

measured result. The only difference is at x = 2,300 (2,300 marked in abscissa which represents a location 2,300 m downstream). There is a tributary merging into the main river from top right of the figure and this stopped the debris flow from going into the tributary at the time of disaster. However, in our simulation, no inflow is assigned from the merging tributary; therefore, debris flow can flow into and is deposited in the lower part of the tributary. Except for the region around the tributary, the maximum error for the boundary of final depositional area is only 20 m. Lastly, we compared the calculated heights of final deposition with measured heights along the cross section marked by solid line in figure 9. The computed result is also close to field measurements as shown in figure 11. The local maximum difference is much lower than 1 m and is well within the accuracy of field measurements.

The good simulation results depend on several factors. First of all, this disaster has a relatively low amount of erosion along the reach, which is consistent with the model. Second, the depth of the debris flow is more than 5 m and the bottom layer is much thinner. However, the small error indicates that the full-scale simulation is good and can reflect the characteristic of the phenomenon.

5. Sensitivity of yield stress and debris volume for field simulation

In field simulations, the most difficult quantity to be found may be the debris volume available from landslide and erosion. Another large error may come from the estimation of rheological parameters for the in situ soil. Assuming the Digital Terrain Model (DTM) is available, we shall compare the sensitivity of the debris volume and yield stress with an actual case in Taiwan in this section.

Chu-Chi is located in the north of Taiwan within Taipei County. A debris flow occurred during typhoon in 1995. The source of the debris flow is a landslide. The source of the landslide is 150 m wide, 50 m high and estimated as 8–10 m deep. The estimated debris volume, V, is about 50,000 m^3 and the average yield stress, τ_0, measured via field samples is 1,000 N/m^2. We compared the effect of increasing V and decreasing τ_0. In both cases, the final front of the debris flow moves further

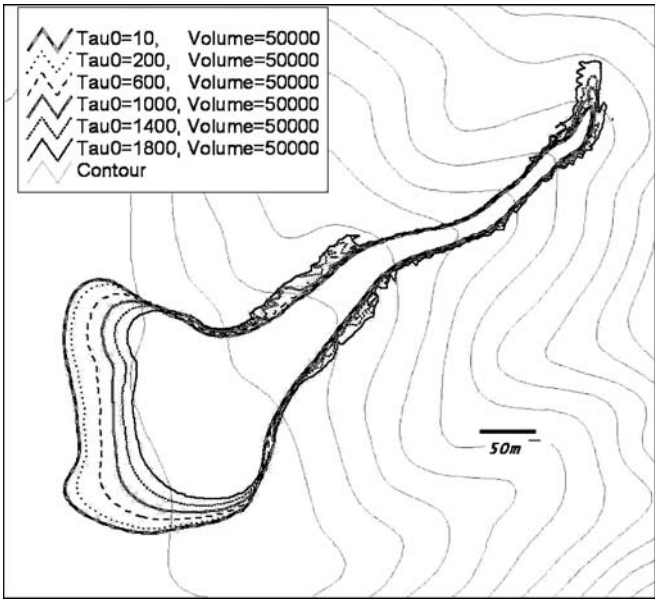

Figure 12. Influence of yield stress in the field. The outermost curve is for the smallest yield stress. Curves from outside to inside is for 0.01, 0.2, 0.6, 1.0, 1.4 and 1.8 times 1,000 N/m^2.

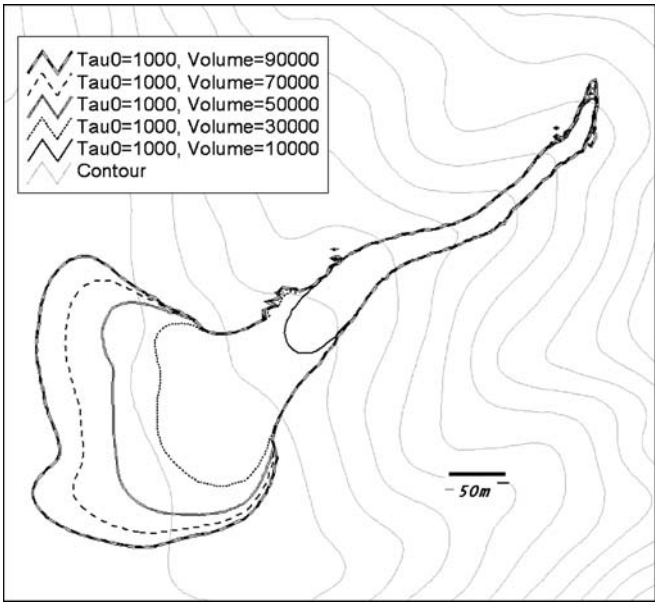

Figure 13. Influence of debris volume in the field. The outermost line is for the largest volume. Curves from outside to inside are for 1.8, 1.4, 1.0, 0.6 and 0.3 times 50,000 m^3.

downstream. We varied both quantities from 80% larger to 80% smaller. Results are shown in figures 12 and 13. The effect of varying V is three to four times larger than the result obtained when we varied τ_0. For example, when V is increased by 40%, the final deposition front moves 45 m downstream. But if τ_0 is decreased by 40%, the final front position moves only 13 m downstream (a difference of more than three times).

A 40% error from yield stress measurement is usually considered large, but 40% error from estimation of available debris volume is common – implying that it is easier to make large error in volume estimation. Combing with the simulated results, it is fair to conclude that simulation results are much more sensitive to debris volume than rheological parameters.

6. Application in Keng-Din stream counter measurements at Taitong, Taiwan

In 1996, serious debris flows occurred in Keng-Ding stream in Taitong County, Taiwan. A total of more than 1 million m^3 debris was accumulated after the debris flow events that lasted about 6 hour, with the main surge concentrating within the first hour. The watershed area is 1,330 ha. The length of the stream is 6.04 km and the total elevation change of the stream is 1.08 km. During planning of the reconstruction of this area, two questions are raised. First, a bridge at the location marked in figure 14 is needed. But how high should the bridge be? Second, if slit dams at the same location are necessary, then what is the estimated impact force? Numerical simulation is used to find the answers.

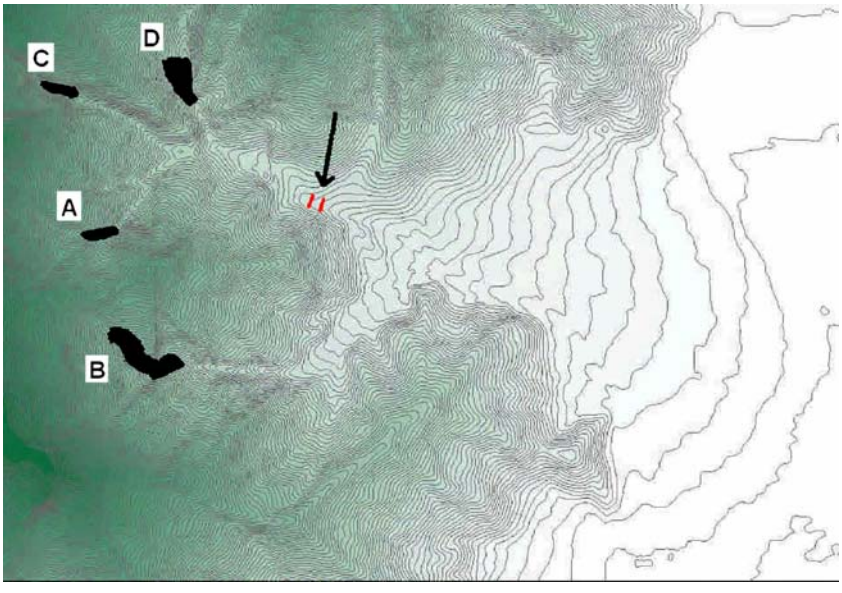

Figure 14. Major landslide area A, B, C and D. The location of slit dams or bridge is marked by an arrow.

Table 2
Estimated soil volume in location marked in figure 14.

Tributary stream	A	B	C	D	Total
Estiated soil volume (in 1,000 m^3)	39	500	36	254	828

Four major locations of landslide are first identified and marked in figure 14, and the corresponding estimated soil volume is obtained through air photo analysis and field verification by the Disaster Prevention Research Center of National Cheng-Kung University, Taiwan. The corresponding estimated soil volume is listed in table 2.

Results from in situ sample tests indicate a density of 1200 kg/cm^3. Yield stress measured by the method described in section 2.3 is 700 N/m^2. The design return period is 50 years, which leads to a rainfall intensity of 161.18 mm/h. Equilibrium concentration is calculated as 0.603. Under the worst-case scenario, all materials that can be mobilized will move; the final deposition profile is plotted in figure 15 as the black area. The boundary conditions used are no-flow conditions upstream of each tributary.

We first use a 10 $\times$ 10 m grid size to simulate the flow to obtain an overall picture. In this grid size, slit dams are too small to be accounted for. Debris flow lasts about 37 min before it stops. Highest deposition occurs at 300 m downstream of the planned slit dams' location and is 12 m deep. Maximum height at the location is 14 m.

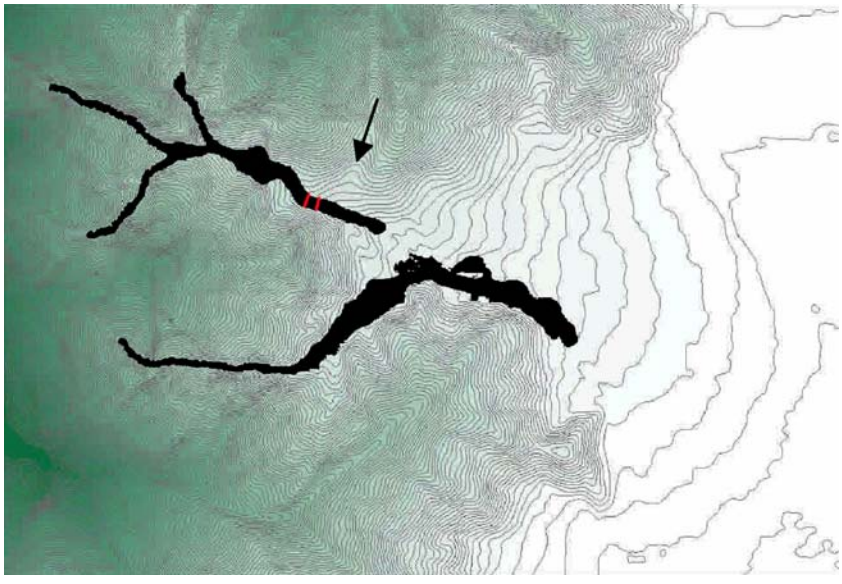

Figure 15. Final deposition of the 50-year return period debris flow event. The location of slit dams or bridge is marked by an arrow.

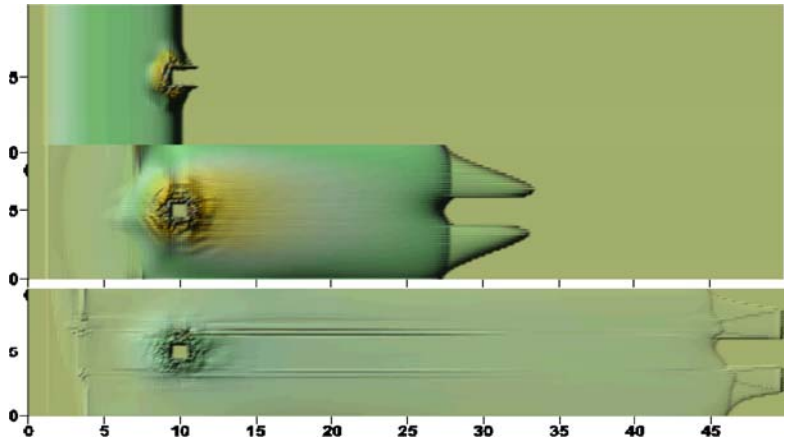

Figure 16. Depth variation of debris flow around the slit. Figures from top to bottom correspond to 50, 200 ad 400 s after impact of debris flow. The grey level represents the depth, the darker the higher.

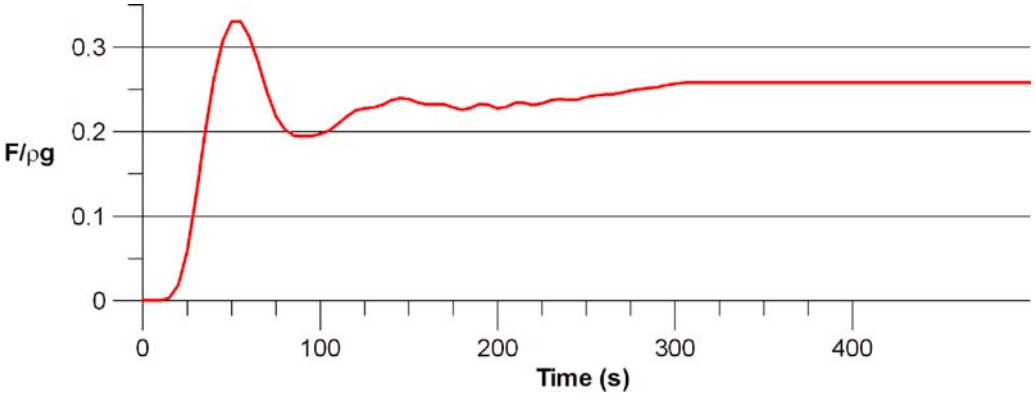

Figure 17. Impact force of debris flow on slit dam.

A bridge passing this potential debris flow stream is thus designed without pier with 16 m net height. Consequently, slit dams will indeed be hit by debris flows. However, the dimension of each slit is 2 m wide and 2 m long, with 3-m spacing. To account for the effect of slit dams and to calculate the impact force, we adopt a finer grid size (1 $\times$ 1 m) from 30 m upstream of the slit dam to 30 m downstream. As a consequence, it now becomes necessary for numerical simulation to be separated into two stages for each time step. At the first stage, the 10 $\times$ 10 m grid size is used. At the next stage, the calculated result is interpolated to give the boundary conditions for finer grids. The calculation iterates once. The depth variation around slit dams during the impact of debris flow is plotted in figure 16. The impact force is plotted in figure 17. Since debris flow is decelerating towards a complete stop, the maximum impact force is only 0.34

$\rho g/m^2$ and is essentially the hydrostatic pressure force. The impact force of huge boulder carried in the front of debris flow can be calculated using the empirical formula given by Takahashi [18].

7. Conclusion

We adopt the concept of separating the boundary layer and the main flow in fluid mechanics to debris flows. By defining the bottom layer of debris flow as a region with stress greater than yield stress, we derived the governing equations in a conservative form. Numerical scheme is verified with analytical solutions and flume tests. Verification by real events also achieves good agreements in the final deposition boundary and depth. The final example demonstrates the usefulness of such a program.

Acknowledgment

This research is supported by National Science Council project NSC89-2625-Z-002-044.

References

[1] R.A. Bagnold, Experiments on a gravity-free dispersion of large solid spheres in a Newtonian fluid under shear, Proc. R. Soc. Lond. 225 (1954) 49–63.
[2] N.J. Balmforth and J.J. Liu, Roll waves in mud, J. Fluid Mech. 519 (2004) 33–54.
[3] C.T. Chang, Rheological measurements in a rotating drum with Bingham type material, Master thesis, National Taiwan University (2004).
[4] P. Coussot and S. Proust, Slow, unconfined spreading of a mud flow. J. Geophys. Res. 101(B11) (1996) 25217–25229.
[5] X. Huang and M.H. Garcia, A Herschal–Hulkley model for mud flow down a slope, J. Fluid Mech. 374 (1998) 305–333.
[6] R.M. Iverson, T.J. Denlinger, R.G. LaHusen and M. Logan, Two-phase debris-flow across 3-D terrain: Model prediction and experimental tests, in: *Proceedings of the 2nd International Conference on Debris Flow Hazards Mitigation,* Taipei, Taiwan, Aug. 16–18 (2000), pp. 521–530.
[7] A.M. Johnson, *Physical Processes in Geology* (Freeman, New York, 1970).
[8] P.Y. Julien and Y. Lan, Rheology of hyperconcentrations, J. Hydraul. Eng. ASCE 117 (1991) 346–353.
[9] K.F. Liu and M.T. Huang, Study of the front shape of 3-D stationary debris flows, in: *Proceedings of 8th Civil and Hydraulic Conference*, Taipei, July 8–9, 1996 (1996) pp. 529–536.
[10] K.F. Liu and M.T. Huang, Three-dimensional numerical simulation of debris flows and its applications, in: *The 3rd International Conference on Debris-Flow Hazards Mitigation*, Sept. 16–18 (2003), pp. 469–481
[11] K.F. Liu and K.W. Lai, Numerical simulation of two-dimensional debris flows, in: *Proceedings of the 2nd International Conference on Debris Flow Hazards Mitigation*, Taipei, Taiwan, Aug. 16–18 (2000), pp. 531–535.

[12] K.F. Liu and C.C. Mei, Slow spreading of a sheet of Bingham fluid on an inclined plane, J. Fluid Mech. 207 (1989) 505–529.
[13] K.F. Liu and F.C. Lee, Experimental analysis on impact mechanism of granular flows, Chin. J. Mech. 13(1) (1997) 87–100.
[14] S. Longo and A. Lamberti, Grain shear flow in a rotating drum, Exp. Fluids 32 (2003) 313–325.
[15] C.C. Mei and M. Yuhi, Slow flow of a Bingham fluid in a shallow channel of finite width, J. Fluid Mech. 431 (2001) 135–159.
[16] C. Ng and C.C. Mei, Roll waves on a shallow layer of mud modeled as a power-law fluid, J. Fluid Mech. 263 (1994) 151–183.
[17] J.S. O'Brien, and P.Y. Julien, On the importance of mudflow routing, in: *Proceedings of the 2nd International Conference on Debris Flow Hazards Mitigation*, Taipei, Taiwan, Aug. 16–18 (2000), pp. 677–686.
[18] T. Takahashi, Debris flow, Int. Assoc. Hydraul. Res. (1991).
[19] Y.F. Tsai, Study on the configuration of debris-flow fan, Ph.D. dissertation, Department of Hydraulic and Ocean Engineering, National Cheng-Kung University, Taiwan (1999).